

Electronic spectrum of twisted bilayer grapheneA. O. Sboychakov,^{1,2} A. L. Rakhmanov,^{1,2,3,4} A. V. Rozhkov,^{1,2,3} and Franco Nori^{1,5}¹*CEMS, RIKEN, Wako-shi, Saitama 351-0198, Japan*²*Institute for Theoretical and Applied Electrodynamics, Russian Academy of Sciences, Moscow 125412, Russia*³*Moscow Institute of Physics and Technology, Dolgoprudny, Moscow Region 141700, Russia*⁴*All-Russia Research Institute of Automatics, Moscow 127055, Russia*⁵*Department of Physics, University of Michigan, Ann Arbor, Michigan 48109-1040, USA*

(Received 23 July 2014; revised manuscript received 16 June 2015; published 3 August 2015)

We study the electronic properties of twisted bilayer graphene in the tight-binding approximation. The interlayer hopping amplitude is modeled by a function which depends not only on the distance between two carbon atoms, but also on the positions of neighboring atoms as well. Using the Lanczos algorithm for the numerical evaluation of eigenvalues of large sparse matrices, we calculate the bilayer single-electron spectrum for commensurate twist angles in the range $1^\circ \lesssim \theta \lesssim 30^\circ$. We show that at certain angles θ greater than $\theta_c \approx 1.89^\circ$ the electronic spectrum acquires a finite gap, whose value could be as large as 80 meV. However, in an infinitely large and perfectly clean sample the gap as a function of θ behaves nonmonotonously, demonstrating exponentially large jumps for very small variations of θ . This sensitivity to the angle makes it impossible to predict the gap value for a given sample, since in experiment θ is always known with certain error. To establish the connection with experiments, we demonstrate that for a system of finite size \tilde{L} the gap becomes a smooth function of the twist angle. If the sample is infinite, but disorder is present, we expect that the electron mean-free path plays the same role as \tilde{L} . In the regime of small angles $\theta < \theta_c$, the system is a metal with a well-defined Fermi surface which is reduced to Fermi points for some values of θ . The density of states in the metallic phase varies smoothly with θ .

DOI: [10.1103/PhysRevB.92.075402](https://doi.org/10.1103/PhysRevB.92.075402)

PACS number(s): 73.22.Pr, 73.21.Ac

I. INTRODUCTION

Bilayer graphene is attracting considerable attention. Recent experimental studies (including scanning tunneling microscopy [1–4], Raman [5,6], and angular resolved photoemission spectroscopy [7,8]) revealed that, in many cases, the structure of bilayer samples is far from the ideal *AB* stacking and is characterized by a nonzero twist angle θ between graphene layers. The physics of twisted bilayer graphene (tBLG) is very rich. The system demonstrates Dirac spectrum with a θ -dependent Fermi velocity [1,5], low-energy Van Hove singularities [3,4], and other interesting features [9,10].

The theoretical description of the low-energy electronic properties of twisted bilayer graphene is based on the notion that for certain, so-called “commensurate,” values of θ , the tBLG lattice may be thought of as a periodic repetition of supercells, containing a large number of carbon atoms. For such angles, numerical studies based on density functional theory and tight-binding calculations [11–19] were performed. Since the number of atoms in an elementary unit cell of the tBLG superlattice may be quite substantial, especially at small twist angles, the *ab initio* calculations incur a significant computational cost. Therefore, the use of such approaches is quite limited. To avoid this difficulty, several semianalytical theories have been developed for describing the low-energy electronic properties of the tBLG [20–26].

These low-energy theories operate mainly with the electronic states near the Dirac cones, which the tBLG inherits from its two constituent layers. In the tBLG, the Dirac cones with equal chirality are located close to each other in momentum space. The interlayer hopping couples these cones and suppresses the Fermi velocity [1,5], which becomes a function of θ .

If subtler effects are of interest [24], a term hybridizing these Dirac cones must be added to the effective long-wave Hamiltonian of the tBLG. The corresponding electronic spectrum obtained is gapped or gapless depending on the type of commensurate structure.

When the twist angle is small ($\theta \lesssim 2^\circ$), the electronic structure changes qualitatively. The picture with Dirac cones becomes irrelevant. Instead, the system acquires a finite density of states at the Fermi level [22].

Yet, despite definite progress, several important theoretical issues remain unaddressed. For example, the regime of low-twist angles received very limited attention. The regime of larger angles was studied in more detail. However, the current understanding of this limit is not without discrepancies. The types of spectra predicted in Ref. [24] do not coincide with those obtained by tight-binding calculations [16]. The value of the single-electron gap was evaluated for several commensurate twist angles, see Refs. [14,16,24]; nonetheless, the generic dependence of the gap on θ was not discussed.

Here we report the results of tight-binding calculations of the band structure of tBLG in a wide range of twist angles. To tackle the issue of the large supercell size we use the Lanczos algorithm, which allows us to calculate the low-energy single-electron spectrum of tBLG. We find that the tBLG single-electron properties are qualitatively different for θ larger and smaller than the critical angle $\theta_c \approx 1.89^\circ$. When $\theta > \theta_c$, the low-energy spectrum can be considered roughly as consisting of two doubly degenerate Dirac cones located near two Dirac points in the Brillouin zone of the superlattice. The Fermi velocity of Dirac electrons is a continuous function of the twist angle θ , and it decreases when θ decreases. This result is in agreement both with the low-energy theories [21–23] and the tight-binding calculations, reported elsewhere [14,17,19].

Under more scrutiny the spectrum reveals its fine structure: the double degeneracy of the single-electron bands is weakly lifted, and for the momenta close to the Dirac points the dispersion deviates from massless Dirac spectrum. The spectrum of the tBLG can be gapped or gapless depending on the type of superstructure, but for any superstructure the band splitting is nonzero. The maximum value of the band gap is estimated to be 80 meV. It corresponds to the twist angle $\theta \cong 21.79^\circ$.

However, in contrast to the Fermi velocity, the band splitting is a discontinuous function of the twist angle. It can change exponentially, even for small variations of θ . Such a feature makes it difficult to predict the gap value for real samples, whose twist angles are always known with some nonzero error. It is demonstrated that this sensitivity of the gap to small variations of the angle is absent for a sample of finite size. The relevance of this “smoothing” for experiment is discussed.

At the critical angle $\theta_c \cong 1.89^\circ$, the Fermi velocity vanishes, and for $\theta < \theta_c$ the conelike structure of the low-energy bands becomes irrelevant. Instead, the system has a finite density of states and a Fermi surface. The Fermi surface changes smoothly as a function of θ .

The presentation below is organized as follows. In Sec. II we briefly discuss the geometry of the tBLG lattice. In Sec. III the tight-binding Hamiltonian is introduced. In Sec. IV the case of large twist angles is discussed. Small θ are discussed in Sec. V. Conclusions are presented in Sec. VI.

II. GEOMETRICAL CONSIDERATIONS

Each graphene layer in the tBLG consists of two sublattices ($A1, B1$ in layer 1, and $A2, B2$ in layer 2). The positions of the carbon atoms in each sublattice in the bottom layer 1 are

$$\mathbf{r}_n^{1A} \equiv \mathbf{r}_n = n\mathbf{a}_1 + m\mathbf{a}_2, \quad \mathbf{r}_n^{1B} = \mathbf{r}_n + \boldsymbol{\delta}_1, \quad (1)$$

where $\mathbf{n} = \{n, m\}$ (n, m are integers), $\boldsymbol{\delta}_1 = (\mathbf{a}_1 + \mathbf{a}_2)/3 = a\{1/\sqrt{3}, 0\}$, and $\mathbf{a}_{1,2}$ are basis vectors of the graphene elementary unit cell,

$$\mathbf{a}_1 = a\{\sqrt{3}, -1\}/2, \quad \mathbf{a}_2 = a\{\sqrt{3}, 1\}/2, \quad (2)$$

with the lattice parameter $a = 2.46 \text{ \AA}$. When the layers are not rotated ($\theta = 0$), the system is a perfect AB bilayer.

Throughout our discussion we will assume that the constituent graphene layers are perfectly flat, and separated by the distance $d = 3.35 \text{ \AA}$ from each other. In a real tBLG sample the layers are not purely two dimensional. The interlayer distance varies [3] depending on local arrangement of the atoms. The interlayer corrugation is quite small ($\sim 0.1 \text{ \AA}$), thus, it can be neglected.

Layer 2 is rotated with respect to layer 1 by the angle θ around the axis connecting the atoms $A1$ and $B2$ with $\mathbf{n} = 0$ (see Fig. 1). In this case the atoms of the top layer have the positions

$$\mathbf{r}_n^{2B} \equiv \mathbf{r}'_n = n\mathbf{a}'_1 + m\mathbf{a}'_2, \quad \mathbf{r}_n^{2A} = \mathbf{r}'_n - \boldsymbol{\delta}_2, \quad (3)$$

where

$$\mathbf{a}'_{1,2} = \mathbf{a}_{1,2} \left(\cos \theta \mp \frac{\sin \theta}{\sqrt{3}} \right) \pm \mathbf{a}_{2,1} \frac{2 \sin \theta}{\sqrt{3}}, \quad (4)$$

and $\boldsymbol{\delta}_2 = a\{\cos \theta, \sin \theta\}/\sqrt{3}$.

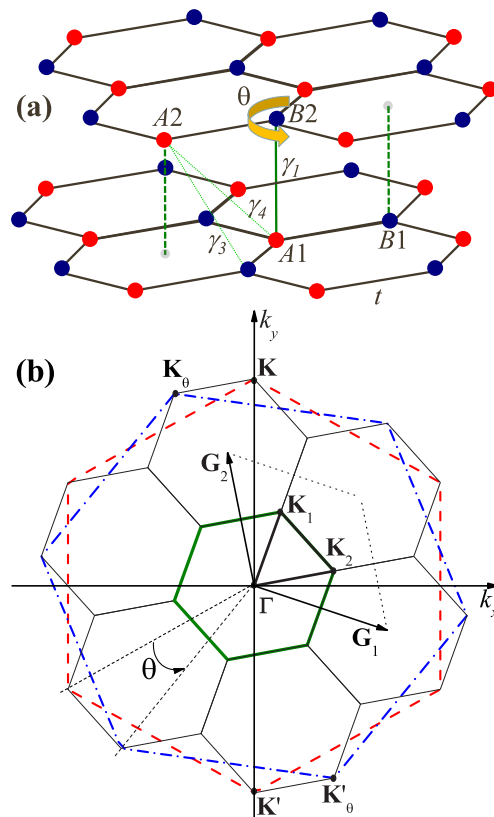


FIG. 1. (Color online) (a) Structure of the AB -stacked graphene bilayer. A twisted graphene bilayer is obtained by rotating the top layer by an angle θ around the axis connecting sites $A1$ and $B2$; quantity t is the in-plane nearest-neighbor hopping, and γ_1, γ_3 , and γ_4 are out-of-plane hopping amplitudes of the AB -stacked bilayer. These γ s are used to fix the fitting parameters of the function $t_{\perp}(\mathbf{r}; \mathbf{r}')$ (see the text). In this paper we use $\gamma_1 = 0.4 \text{ eV}$, $\gamma_3 = 0.254 \text{ eV}$, and $\gamma_4 = 0.051 \text{ eV}$. (b) The large hexagons show the Brillouin zones of individual layers: the dashed hexagon (red) corresponds to the bottom layer, the dot-dashed hexagon (blue) corresponds to the top layer for the twist angle $\theta = 21.787^\circ$ ($m_0 = 1, r = 1$). The first Brillouin zone of the bilayer is shown by the central (green) thick solid hexagon. The next several Brillouin zones of the tBLG are depicted by the six surrounding (black) thin solid hexagons. The electronic spectra presented in Fig. 2 are calculated along the path specified by the triangle $\Gamma\mathbf{K}_1\mathbf{K}_2$ (black). For the twisted bilayer, the Dirac point \mathbf{K}' (\mathbf{K}'_{θ}) is equivalent to the point \mathbf{K}_{θ} (\mathbf{K}) if $r \neq 3n$. When $r = 3n$, $\mathbf{K}_{\theta} \sim \mathbf{K}$ and $\mathbf{K}'_{\theta} \sim \mathbf{K}'$ (see the text). The tBLG Dirac points $\mathbf{K}_{1,2}$ are doubly degenerate: each of them is equivalent to one of two Dirac points of each graphene layer. For the particular case of the $(1,1)$ superstructure, $\mathbf{K}_1 \sim \mathbf{K} \sim \mathbf{K}'_{\theta}$ and $\mathbf{K}_2 \sim \mathbf{K}' \sim \mathbf{K}_{\theta}$.

The structure of the tBLG is commensurate if [13,20–22]

$$\cos \theta = \frac{3m_0^2 + 3m_0r + r^2/2}{3m_0^2 + 3m_0r + r^2}, \quad (5)$$

where m_0 and r are coprime positive integers. The superlattice vectors, $\mathbf{R}_{1,2}$, can be expressed via m_0, r , and the single-layer graphene lattice vectors, $\mathbf{a}_{1,2}$. These expressions are different when r is either nondivisible or divisible by 3. In the former

case, we have

$$\begin{aligned}\mathbf{R}_1 &= m_0\mathbf{a}_1 + (m_0 + r)\mathbf{a}_2 \\ \mathbf{R}_2 &= -(m_0 + r)\mathbf{a}_1 + (2m_0 + r)\mathbf{a}_2\end{aligned}\quad (r \neq 3n, n \in \mathcal{N}). \quad (6)$$

For $r = 3n$, the superlattice vectors become

$$\begin{aligned}\mathbf{R}_1 &= (m_0 + n)\mathbf{a}_1 + n\mathbf{a}_2 \\ \mathbf{R}_2 &= -n\mathbf{a}_1 + (m_0 + 2n)\mathbf{a}_2\end{aligned}\quad (r = 3n, n \in \mathcal{N}). \quad (7)$$

The number of sites in each supercell is

$$N(m_0, r) = \begin{cases} 4(3m_0^2 + 3m_0r + r^2), & \text{if } r \neq 3n, \\ 4(m_0^2 + m_0r + r^2/3), & \text{if } r = 3n. \end{cases} \quad (8)$$

The linear size of the superlattice cell (SC) is

$$L_{sc} \equiv |\mathbf{R}_{1,2}| = a\sqrt{N}/2. \quad (9)$$

Besides L_{sc} , the tBLG has another characteristic length scale. The rotation of one graphene layer with respect to another one leads to the appearance of Moiré patterns, which manifest themselves as alternating bright and dark regions in STM images [1–4]. The Moiré period L , is defined as the distance between centers of two neighboring bright (or dark) regions. It is related to the twist angle according to the following formula:

$$L = \frac{a}{2 \sin(\theta/2)}. \quad (10)$$

The Moiré pattern and the superstructure are two complementary concepts used to describe tBLG. The Moiré pattern depends smoothly on the twist angle; see, e.g., Eq. (10). The pattern can be easily detected experimentally. However, working with the Moiré theoretically may be challenging due to the fact that the pattern is strictly periodic only for a very limited discrete set of angles. For a generic value of θ , different Moiré cells in a pattern may look alike, but they are not exactly identical.

The superstructure, which is a periodic lattice of supercells, does not suffer from this shortcoming. Unfortunately, it has its own deficiencies. Namely, the superstructure is only defined for commensurate angles θ . The period L_{sc} is not a smooth function of θ : two commensurate θ and θ' , $\theta \approx \theta'$, may correspond to two very dissimilar L_{sc} . As we will see below, such sensitivity to the twist angle may, in some situations, require additional efforts in interpreting theoretical results.

One can easily demonstrate that the superstructure coincides with the Moiré pattern only when $r = 1$. For other superstructures, L_{sc} is greater than L . The supercells of these structures contain r^2 (if $r \neq 3n$) or $r^2/3$ (if $r = 3n$) Moiré cells, and the arrangements of atoms inside these Moiré cells are slightly different from each other. This means, in particular, that the structures with $r > 1$ can be considered as almost periodic repetitions of structures with $r = 1$, as it was shown in Ref. [22].

The basis vectors of the reciprocal superlattice can be written as

$$\begin{aligned}\mathbf{G}_1 &= \frac{(2m_0 + r)\mathbf{b}_1 + (m_0 + r)\mathbf{b}_2}{3m_0^2 + 3m_0r + r^2}, \\ \mathbf{G}_2 &= \frac{-(m_0 + r)\mathbf{b}_1 + m_0\mathbf{b}_2}{3m_0^2 + 3m_0r + r^2},\end{aligned} \quad (11)$$

if $r \neq 3n$, or

$$\begin{aligned}\mathbf{G}_1 &= \frac{(m_0 + 2n)\mathbf{b}_1 + n\mathbf{b}_2}{m_0^2 + m_0r + r^2/3}, \\ \mathbf{G}_2 &= \frac{-n\mathbf{b}_1 + (m_0 + n)\mathbf{b}_2}{m_0^2 + m_0r + r^2/3},\end{aligned} \quad (12)$$

if $r = 3n$, where

$$\mathbf{b}_1 = 2\pi\{1/\sqrt{3}, -1\}/a, \quad \mathbf{b}_2 = 2\pi\{1/\sqrt{3}, 1\}/a \quad (13)$$

are the reciprocal-lattice vectors of the single-layer graphene. The first Brillouin zone of the superlattice has the shape of a hexagon with sides $|\mathbf{G}_2 - \mathbf{G}_1|/3$. In the particular case of $r = 1$, this side is equal to $\Delta K = |\mathbf{K}_\theta - \mathbf{K}|$, where

$$\mathbf{K} = \frac{4\pi}{3}\{0, 1\} \quad \text{and} \quad \mathbf{K}_\theta = \frac{4\pi}{3}\{-\sin\theta, \cos\theta\} \quad (14)$$

are the Dirac points of the bottom and top layers, respectively.

As known from basic graphene tight-binding physics, in addition to the Dirac cone at the \mathbf{K} point, the bottom layer of the tBLG has another cone of opposite chirality at $\mathbf{K}' = -\mathbf{K}$. Likewise, the top layer has its second cone at $\mathbf{K}'_\theta = -\mathbf{K}_\theta$. It is important to determine where these two cones are located in the Brillouin zone of the superstructure. To find this out we express their coordinates in terms of reciprocal superlattice vectors. For $r \neq 3n$ we have

$$\begin{aligned}\mathbf{K} &= -\mathbf{K}' = m_0\mathbf{G}_2 + \frac{r}{3}(\mathbf{G}_1 + 2\mathbf{G}_2), \\ \mathbf{K}_\theta &= -\mathbf{K}'_\theta = m_0\mathbf{G}_2 + \frac{r}{3}(\mathbf{G}_2 - \mathbf{G}_1),\end{aligned} \quad (15)$$

while for $r = 3n$ we obtain

$$\begin{aligned}\mathbf{K} &= -\mathbf{K}' = \frac{r}{3}\mathbf{G}_2 + \frac{m_0}{3}(\mathbf{G}_2 - \mathbf{G}_1), \\ \mathbf{K}_\theta &= -\mathbf{K}'_\theta = -\frac{r}{3}\mathbf{G}_1 + \frac{m_0}{3}(\mathbf{G}_2 - \mathbf{G}_1).\end{aligned} \quad (16)$$

It follows from these formulas that, if $r \neq 3n$, point \mathbf{K}' is equivalent to \mathbf{K}_θ , and \mathbf{K} is equivalent to \mathbf{K}'_θ : for such a value of r the difference $\mathbf{K}' - \mathbf{K}_\theta$ is a reciprocal vector of the superlattice. When $r = 3n$, the equivalent Dirac points are $\mathbf{K} \sim \mathbf{K}_\theta$ and $\mathbf{K}' \sim \mathbf{K}'_\theta$. Thus, for any commensurate angle we have two doubly degenerate nonequivalent Dirac points of the tBLG. It follows from Eqs. (15) and (16) that inside the reciprocal cell of the superlattice, the two nonequivalent tBLG Dirac points are located at

$$\mathbf{K}_1 = \frac{\mathbf{G}_1 + 2\mathbf{G}_2}{3}, \quad \mathbf{K}_2 = \frac{2\mathbf{G}_1 + \mathbf{G}_2}{3}, \quad (17)$$

for any superstructure. As we will show below, this double degeneracy affects the electronic structure of the tBLG, leading to band splitting and band-gap formation.

III. TIGHT-BINDING HAMILTONIAN

It is convenient to enumerate the sites in the sublattice in each layer using two integer-valued vectors $\mathbf{j} = \{i, j\}$ and $\mathbf{n} = \{n, m\}$, where \mathbf{j} labels the position of the supercell in the lattice, while \mathbf{n} enumerates the sites inside the supercell. Then, we can write down the tight-binding Hamiltonian of the tBLG

in the form

$$H = -t \sum_{\substack{(\mathbf{i}, \mathbf{j}, \mathbf{m}) \\ s\sigma}} (d_{s\mathbf{i}\mathbf{n}A\sigma}^\dagger d_{s\mathbf{j}\mathbf{m}B\sigma} + \text{H.c.}) \\ + \sum_{\substack{\mathbf{i}, \mathbf{j}, \mathbf{m} \\ \alpha\beta\sigma}} [t_\perp(\mathbf{R}_i + \mathbf{r}_n^{1\alpha}; \mathbf{R}_j + \mathbf{r}_m^{2\beta}) d_{i\mathbf{n}\alpha\sigma}^\dagger d_{j\mathbf{m}\beta\sigma} + \text{H.c.}], \quad (18)$$

where $\mathbf{R}_j = i\mathbf{R}_1 + j\mathbf{R}_2$, the symbol $\langle \dots \rangle$ stands for summation over the nearest neighbors within the same layer, $d_{s\mathbf{j}\mathbf{n}\alpha\sigma}^\dagger$ and $d_{s\mathbf{j}\mathbf{n}\alpha\sigma}$ are the creation and annihilation operators of an electron with the spin projection σ in the layer $s(=1,2)$ on the sublattice $\alpha(=A,B)$ in the supercell \mathbf{j} in the position \mathbf{n} (the position of this site is $\mathbf{R}_j + \mathbf{r}_n^\alpha$). The first term describes the in-plane nearest-neighbor hopping with amplitude $t = 2.57$ eV. The second term describes the interlayer hopping, with $t_\perp(\mathbf{r}; \mathbf{r}')$ being the hopping amplitude between sites in the positions \mathbf{r} and \mathbf{r}' .

This Hamiltonian (18) is invariant with respect to translations by the superstructure vectors $\mathbf{R}_{1,2}$. Performing the Fourier transform $d_{s\mathbf{k}\mathbf{n}\alpha\sigma} = \mathcal{N}_{sc}^{-1/2} \sum_{\mathbf{j}} e^{-i\mathbf{k}\mathbf{R}_j} d_{s\mathbf{j}\mathbf{n}\alpha\sigma}$, where \mathcal{N}_{sc} is the number of supercells in the bilayer, and using the relation $t_\perp(\mathbf{R}_j + \mathbf{r}; \mathbf{R}_j + \mathbf{r}') = t_\perp(\mathbf{r}; \mathbf{r}')$, we obtain

$$H = \sum_{\substack{\mathbf{k}, \mathbf{m} \\ s\sigma}} [t_{\mathbf{nm}}^s(\mathbf{k}) d_{s\mathbf{k}\mathbf{n}A\sigma}^\dagger d_{s\mathbf{k}\mathbf{m}B\sigma} + \text{H.c.}] \\ + \sum_{\substack{\mathbf{k}, \mathbf{m} \\ \alpha\beta\sigma}} [t_{\perp\mathbf{nm}}^{\alpha\beta}(\mathbf{k}) d_{1\mathbf{k}\mathbf{n}\alpha\sigma}^\dagger d_{2\mathbf{k}\mathbf{m}\beta\sigma} + \text{H.c.}], \quad (19)$$

where \mathbf{k} runs over the first Brillouin zone of the superlattice. In Eq. (19)

$$t_{\mathbf{nm}}^s(\mathbf{k}) = -t \sum_{\mathbf{j}\delta} e^{-i\mathbf{k}\mathbf{R}_j} \delta_{\mathbf{N}_j + \mathbf{n}, \mathbf{m} - \delta}, \quad (20)$$

$$t_{\perp\mathbf{nm}}^{\alpha\beta}(\mathbf{k}) = \sum_{\mathbf{j}} e^{-i\mathbf{k}\mathbf{R}_j} t_\perp(\mathbf{R}_j + \mathbf{r}_n^{1\alpha}; \mathbf{r}_m^{2\beta}), \quad (21)$$

the vector δ takes the values $\{0,0\}$, $\{1,0\}$, $\{0,1\}$, and

$$\mathbf{N}_j = \{m_0 i - (m_0 + r)j, (m_0 + r)i + (2m_0 + r)j\}.$$

We use the approach proposed in Ref. [27] to calculate the interlayer hopping amplitudes. The main premise of this approach is that $t_\perp(\mathbf{r}; \mathbf{r}')$ depends not only on the relative positions of the initial and final carbon atoms, but also on the positions of other atoms in the bilayer via the screening function $S(\mathbf{r}; \mathbf{r}')$ [see Eq.(2) in Ref. [27]]; the closer some of the neighboring atoms are to the line connecting the sites \mathbf{r} and \mathbf{r}' , the stronger is the screening. The inclusion of the screening is very important. Otherwise, the longer-range hopping amplitudes in the usual Slonczewski-Weiss-McClure (SWM) scheme [28–31] cannot be correctly reproduced. Without screening, the next-nearest-neighbor interlayer hopping amplitudes of the AB bilayer, γ_3 and γ_4 [see Fig. 1(a)], become identical. This conclusion is at odds with the SWM scheme, where these amplitudes differ by about an order of magnitude.

Following Ref. [27] we write the hopping amplitude in the form

$$t_\perp(\mathbf{r}; \mathbf{r}') = \cos^2 \alpha V_\sigma(\mathbf{r}; \mathbf{r}') + \sin^2 \alpha V_\pi(\mathbf{r}; \mathbf{r}'), \\ \cos \alpha = \frac{d}{\sqrt{d^2 + (\mathbf{r} - \mathbf{r}')^2}}, \quad (22)$$

where the ‘‘Slater-Koster’’ functions V_σ and V_π contain the factor $[1 - S(\mathbf{r}; \mathbf{r}')] [exact expressions for V_σ and V_π are given by Eq. (1) in Ref. [27]]. Calculating hopping amplitudes using Eq. (22) we assume, as explained in Sec. II, that the layers are perfectly flat. In principle, the interlayer distance is not constant, but, rather, changes [3] over the Moiré cell, affecting local t_\perp . However, due to the smallness of such a corrugation, the corresponding variation of t_\perp will be disregarded. Likewise, local distortions of the perfect honeycomb lattice caused by modulation of the interlayer interatomic forces within a single Moiré cell are not accounted by our model.$

Under these assumptions we found that the contribution to t_\perp from V_π is negligible, in agreement with Refs. [15,21,22]. Due to screening, the function $t_\perp(\mathbf{r}; \mathbf{r}')$ decays very quickly when $|\mathbf{r} - \mathbf{r}'| > a$. The functions $V_\sigma(\mathbf{r}; \mathbf{r}')$ and $S(\mathbf{r}; \mathbf{r}')$ in Ref. [27] depend on seven fitting parameters ($\alpha_{1,2,3,4}$ and $\beta_{1,2,3}$). However, the values found in Ref. [27] cannot be directly applied to bilayer graphene [15]. Instead, we use the following estimates for the fitting constants [32]: $\alpha_1 = 6.715$, $\alpha_2 = 0.762$, $\alpha_3 = 0.179$, $\alpha_4 = 1.411$, $\beta_1 = 6.811$, $\beta_2 = 0.01$, and $\beta_3 = 19.176$ (cf. with the third line of Table I of Ref. [27]). With these coefficients we reproduce the well-known SWM hopping amplitudes $\gamma_{1,3,4}$ in the AB bilayer (see Fig. 1 for the definitions of $\gamma_{1,3,4}$). A similar approach was used in Ref. [15], but the authors obtained different fitting parameters because they used another optimization procedure.

We now introduce the N -component operator

$$\Psi_{\mathbf{k}\sigma}^\dagger = \{d_{1\mathbf{k}\mathbf{n}A\sigma}^\dagger, d_{1\mathbf{k}\mathbf{n}B\sigma}^\dagger, d_{2\mathbf{k}\mathbf{n}A\sigma}^\dagger, d_{2\mathbf{k}\mathbf{n}B\sigma}^\dagger\} \quad (23)$$

and rewrite Eq. (19) in the form $H = \sum_{\mathbf{k}\sigma} \Psi_{\mathbf{k}\sigma}^\dagger \hat{H}_{\mathbf{k}} \Psi_{\mathbf{k}\sigma}$, where $\hat{H}_{\mathbf{k}}$ is the $N \times N$ matrix

$$\hat{H}_{\mathbf{k}} = \begin{pmatrix} 0 & \hat{t}_{\mathbf{k}}^1 & \hat{t}_{\perp\mathbf{k}}^{11} & \hat{t}_{\perp\mathbf{k}}^{12} \\ \hat{t}_{\mathbf{k}}^{1\dagger} & 0 & \hat{t}_{\perp\mathbf{k}}^{21} & \hat{t}_{\perp\mathbf{k}}^{22} \\ \hat{t}_{\perp\mathbf{k}}^{11\dagger} & \hat{t}_{\perp\mathbf{k}}^{21\dagger} & 0 & \hat{t}_{\mathbf{k}}^2 \\ \hat{t}_{\perp\mathbf{k}}^{12\dagger} & \hat{t}_{\perp\mathbf{k}}^{22\dagger} & \hat{t}_{\mathbf{k}}^{2\dagger} & 0 \end{pmatrix}. \quad (24)$$

Here, the matrices $\hat{t}_{\mathbf{k}}^s$ and $\hat{t}_{\perp\mathbf{k}}^{\alpha\beta}$ are constructed from $t_{\mathbf{nm}}^s(\mathbf{k})$ and $t_{\perp\mathbf{nm}}^{\alpha\beta}(\mathbf{k})$ according to Eqs. (20) and (21).

The energy spectrum of the tBLG consists of N bands $E_{\mathbf{k}}^{(i)}$ ($i = 1, \dots, N$). We are interested here in the spectrum near the Fermi level μ at half filling. The chemical potential μ is nonzero due to the violation of the particle-hole symmetry of our tight-binding Hamiltonian, and it has to be found with the help of the charge-neutrality requirement. For a rough estimate of μ we use the formula relating the number of electrons per site n_e and chemical potential μ , which does not require the full diagonalization of the matrix $\hat{H}_{\mathbf{k}}$:

$$n_e(\mu) = \frac{2T}{N} \sum_{i\omega} \int \frac{d^2\mathbf{k}}{\nu_{BZ}} e^{i\omega 0^+} \text{Tr} \left[\frac{1}{i\omega + \mu - \hat{H}_{\mathbf{k}}} \right] = 1, \quad (25)$$

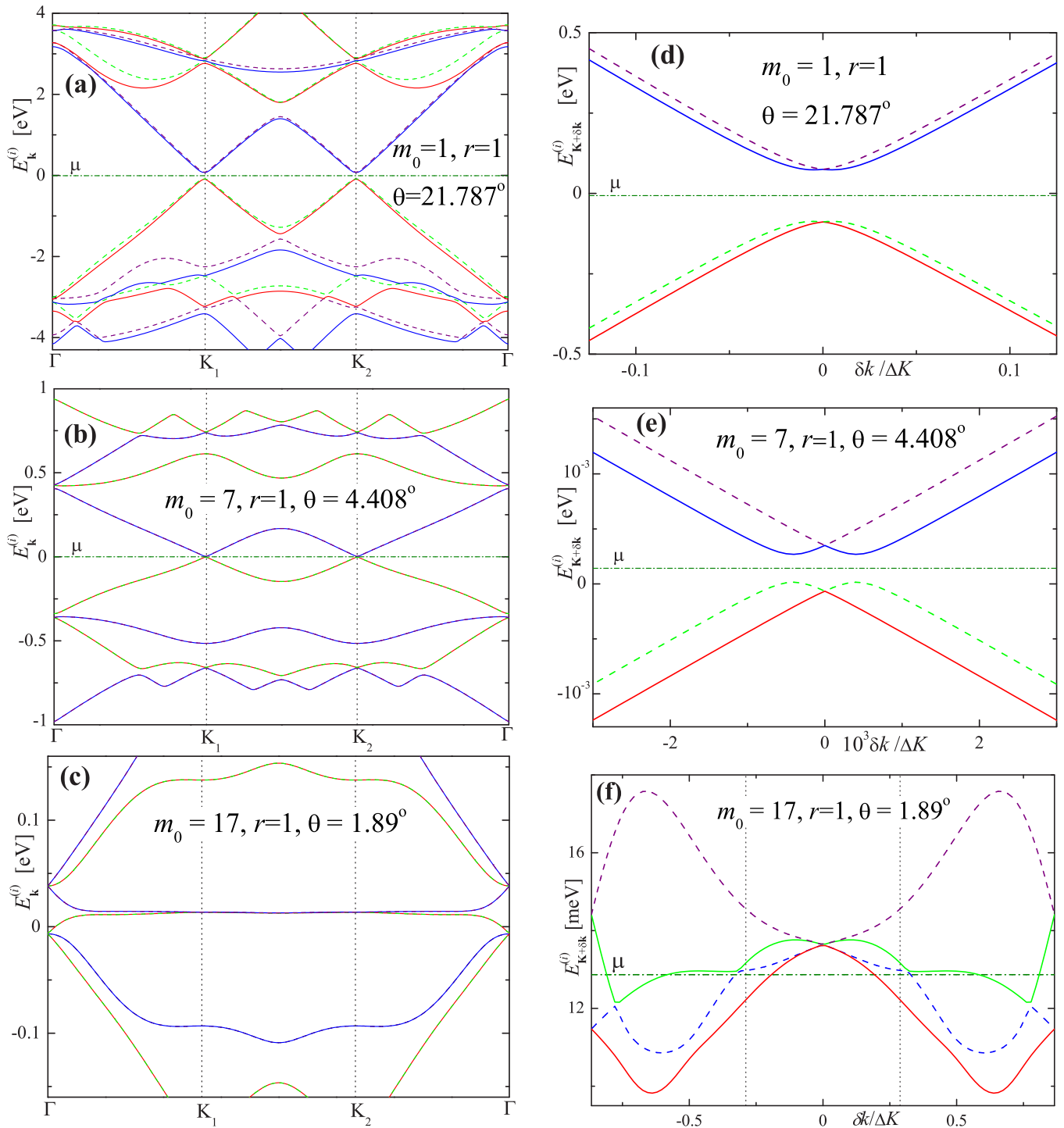


FIG. 2. (Color online) (a)–(c) The spectra of the twisted bilayer graphene calculated for three different twist angles θ along the path $\Gamma\mathbf{K}_1\mathbf{K}_2$ shown in Fig. 1(b). The spectrum shown in panel (a) corresponds to $\theta \approx 21.787^\circ$. It demonstrates a significant gap. The detailed behavior of this spectrum near the Dirac point is shown in panel (d) [the dispersion curves shown in panel (d) and (e) are calculated along the line parallel to vector $\Delta\mathbf{K} = \mathbf{K}_2 - \mathbf{K}_1$]. Two almost-degenerate bands approaching the Fermi level μ from above and two almost-degenerate bands approaching it from below are clearly seen. For a much smaller angle $\theta \approx 4.408^\circ$, panel (b), the gap is much smaller, but still present; see panel (e). Panels (c) and (f) correspond to $\theta \approx 1.89^\circ$. The spectrum is gapless and three bands cross the Fermi energy forming the Fermi surface. The low-energy dispersion shown in panel (f) is calculated along the line passing through the Dirac point \mathbf{K}_2 perpendicular to the vector $\Delta\mathbf{K}$ [the dot-dashed line in Fig. 8(a)]. In panels (d)–(f) the Dirac point corresponds to $\delta\mathbf{k} = 0$.

where v_{BZ} is the area of the first Brillouin zone of the superstructure, the summation is performed over the Matsubara frequencies, and T is the temperature, which we choose low enough ($T = 0.1\gamma_1$). Estimates of μ according to Eq. (25) show that $|\mu|$ is very small for any twist angle, and only n_0 bands with the smallest absolute values, $\bar{E}_{\mathbf{k}}^{(v)} = E_{\mathbf{k}}^{(i_0+v)}$ [$i_0 = (N - n_0)/2 - 2$, $v = 1, \dots, n_0$] can cross the Fermi level. Analysis shows that when $\theta > \theta_c$ the number of low-energy bands is $n_0 = 4$. For $\theta < \theta_c$, we have $n_0 = 4r^2$, if $r \neq 3n$, or $n_0 = 4r^2/3$ otherwise. More precise value of the chemical potential μ is found from the usual charge-neutrality relation:

$$2 \sum_v \int \frac{d^2\mathbf{k}}{v_{\text{BZ}}} \Theta(\mu - \bar{E}_{\mathbf{k}}^{(v)}) = n_0. \quad (26)$$

The distant hopping amplitudes $t_{\perp}(\mathbf{r}; \mathbf{r}')$ turn out to be negligible, and the matrix $\hat{H}_{\mathbf{k}}$ is very sparse; that is, the number of nonzero elements in $\hat{H}_{\mathbf{k}}$ is proportional to N . This allows us to use the Lanczos algorithm to calculate the eigenvalues closest to zero energy [33]. Then we calculate the spectra along the contour in \mathbf{k} space shown in Fig. 1(b) for a set of superstructures with (m_0, r) varying in a broad range.

IV. LARGE TWIST ANGLES $\theta > \theta_c$

A. Superstructures with $r = 1$

We explained in Sec. II that the superstructures with $r > 1$ can be viewed as almost-periodic repetitions of superstructures with $r = 1$. Consequently, some electronic properties of a bilayer with generic values of θ may be easily linked to the properties of a $r = 1$ system. This makes the study of the $r = 1$ case particularly useful. Below we calculate the spectra for several such superstructures: we vary m_0 from $m_0 = 1$ ($\theta = 21.787^\circ$, the number of sites in the supercell $N = 28$) to $m_0 = 25$ ($\theta = 1.297^\circ$, $N = 7804$). The results for three different angles are shown in Figs. 2(a)–2(c). The results are qualitatively different for θ larger and smaller than the critical value $\theta_c \cong 1.89^\circ$ corresponding to $m_0 = 17$.

For $r = 1$ the number of low-energy bands $n_0 = 4$ for any θ . When $\theta > \theta_c$ ($m_0 < 17$), two pairs of bands come close to the Fermi level μ in the vicinity of the tBLG Dirac points \mathbf{K}_1 and \mathbf{K}_2 : one pair from below and another pair from above. The bands in each pair are almost degenerate in a large range of momentum space. The smaller θ , the smaller the energy difference between bands in these pairs. Neither of the bands reach the Fermi energy for $\theta > \theta_c$. Thus, in this case the system is an insulator with a nonzero band gap Δ . Near the Dirac points $\mathbf{K}_{1,2}$, at $\mathbf{k} = \mathbf{K}_{1,2} + \delta\mathbf{k}$, the energy spectrum can be approximated as

$$\bar{E}_{\mathbf{K}_{1,2}+\delta\mathbf{k}}^{(v)} = \mu \pm \sqrt{\Delta^2 + v_F^2(|\delta\mathbf{k}| \pm k_0)^2}, \quad (27)$$

where the different signs correspond to different bands; Δ , v_F , and k_0 are fitting parameters [see Figs. 2(d) and 2(e)]. The quantities Δ and v_F , calculated by fitting the numerical data for $\bar{E}_{\mathbf{k}}^{(v)}$ using Eq. (27), are shown in Fig. 3 as functions of θ . The gap monotonously decreases when θ decreases, with a single exception at $\theta \cong 9.43^\circ$ ($m_0 = 3$). The gap $\Delta \gtrsim 1$ K if $\theta \gtrsim 4.408^\circ$ ($m_0 \leq 7$) and achieves the value $\Delta \cong 0.08$ eV when $\theta \cong 21.787^\circ$ ($m_0 = 1$). Thus, it can be experimentally

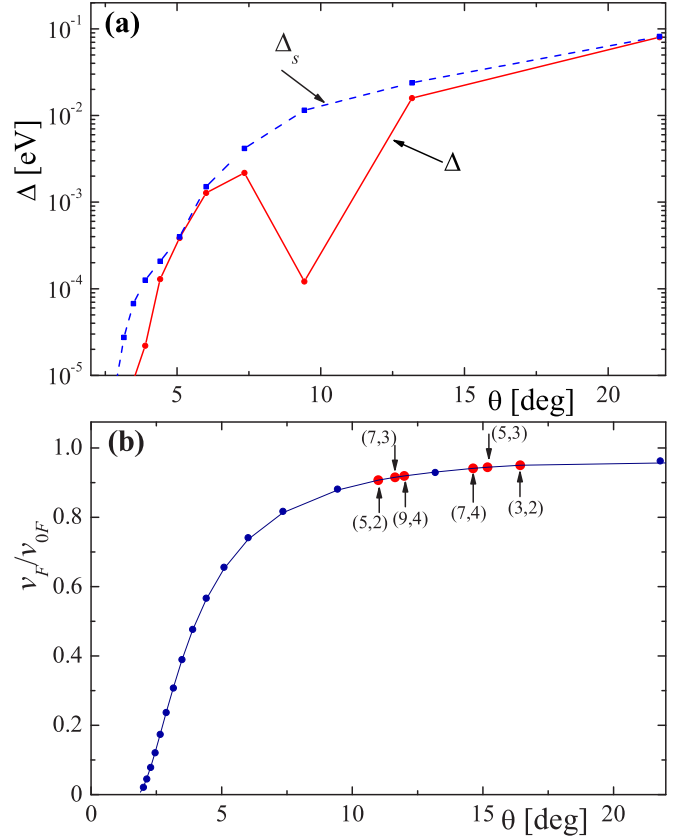


FIG. 3. (Color online) Single-electron spectrum properties as functions of the twist angle θ . In panel (a) the dependencies of the band gap Δ (red solid curve) and band splitting Δ_s (blue dashed curve) are shown for $r = 1$ structures. In panel (b) the Fermi velocity v_F for both $r = 1$ structures (small blue dots), and $r \neq 1$ structures (larger red dots) is plotted. To extract the gap Δ , splitting Δ_s , and Fermi velocity v_F , the numerically determined low-energy bands $\bar{E}_{\mathbf{k}}^{(v)}$ were fitted by Eq. (27).

measured if the twist angle is not small. In the region $\theta_c < \theta \lesssim 4.4^\circ$, the gap is too small, and one can consider the tBLG to be a semimetal. The spectrum of the tBLG with a gap was observed in recent experiments [8]. However, the nature of this gap is unclear.

If we neglect the values Δ and k_0 in Eq. (27), the band structure reduces to two doubly degenerate Dirac cones located at the points \mathbf{K}_1 and \mathbf{K}_2 and intersecting at higher energies. The Fermi velocity v_F is smaller than that of the single-layer graphene, $v_{0F} = ta\sqrt{3}/2$, and it monotonously decreases with decreasing twist angle (see Fig. 3). This picture is quite consistent with many previous studies utilizing different approaches [13–17, 19–23].

The gap may be viewed as a consequence of hybridization between the states located at the Dirac points of two graphene layers \mathbf{K}_θ and \mathbf{K}' (and \mathbf{K} and \mathbf{K}'_θ). Indeed, as it was mentioned above, for commensurate structures with $r \neq 3n$ the momenta \mathbf{K}' and \mathbf{K}_θ are equivalent to each other [see Eq. (15)]. The matrix element mixing the states near \mathbf{K}_θ and \mathbf{K}' is allowed by symmetry, which leads to the band splitting and gap opening.

This hybridization is ignored in the continuum approximations [21–23], even though Refs. [21, 22] mentioned such

a possibility. The phenomenological approach taking into account the hybridization between different Dirac cones in the tBLG was proposed in Ref. [24]. However, if $r = 1$, as we assume in this subsection, the formalism of Ref. [24] predicts a gapless spectrum, failing to capture the insulating state of $r = 1$ structures.

A more general result of the hybridization between electron states near the Dirac points is the breakdown of the double degeneracy of the low-energy bands of the tBLG. For $r = 1$ structures, the band gap Δ would be the measure of such a band splitting. However, this is not so for structures with $r = 3n$, where the gap is zero as we will show below. Here, following Refs. [14,16], we introduce the quantity

$$\Delta_s = (\bar{E}_{\mathbf{K}}^{(4)} - \bar{E}_{\mathbf{K}}^{(1)})/2 \quad (28)$$

as a measure of this band splitting. According to Eq. (27), Δ and Δ_s satisfy the relationship

$$\Delta_s = \sqrt{\Delta^2 + v_F^2 k_0^2}.$$

The dependence of Δ_s on θ is also shown in Fig. 3. In contrast to the band gap, Δ_s monotonously decreases with the twist angle θ .

The tight-binding calculations in Refs. [14,16] predicted the existence of the band splitting in the tBLG. However, the value of Δ_s is at least one order of magnitude smaller than our value (cf. Fig. 3 with Fig. 9 in Ref. [14], or with Fig. 1 in Ref. [16]). We attribute this discrepancy to the different choice of the function $t_{\perp}(\mathbf{r}; \mathbf{r}')$. We believe that our choice is more suitable for the tBLG since it reproduces the SWM hopping parameters for AB bilayer graphene. A similar conclusion was reached in Ref. [25]. Our calculations show, that if we neglect the environment dependence of the hopping, leading to the difference between γ_3 and γ_4 hopping amplitudes of the AB bilayer, the gap for the tBLG becomes smaller, and we reproduce the results of Refs. [14,16]. The value Δ_s estimates the band splitting near the Dirac point. However, it can be substantially larger in other regions of momentum space. The band splitting was experimentally observed by ARPES measurements in Ref. [7].

B. Superstructures with $r \neq 1$

The superstructures with $r = 1$, considered in the previous subsection, exhaust a fairly limited set of twist angles. Can the knowledge about this set be sufficient to adequately capture the properties of the tBLG for a generic value of θ ? The answer to this question is positive, if one aims to describe the Fermi velocity (see, for example, Fig. 3). However, as we will see below, it is negative, if one needs to know the band gap. Therefore, a detailed study of $r \neq 1$ systems is required.

The supercell of the structure (m_r, r) with $r > 1$ contains r^2/g Moiré cells, where $g = 1$ if $r \neq 3n$, or $g = 3$ otherwise. The arrangements of carbon atoms inside these cells are slightly different from each other and approximately correspond to the $r = 1$ superstructure with $m_0 = [m_r/r]$, where $[a]$ means the integer part of a . Since these structures are not completely identical, this can affect the electronic structure of the tBLG. In this subsection we consider the differences and similarities between electronic spectra of “basic” $r = 1$ structures and superstructures with $r > 1$.

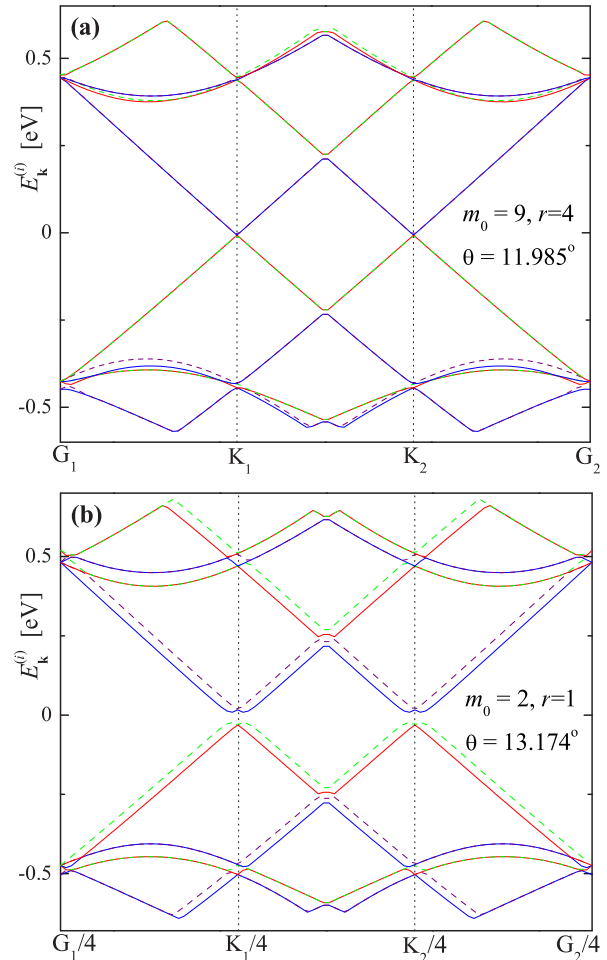


FIG. 4. (Color online) The spectra of the twisted bilayer graphene calculated for structures (9,4) (a) and (2,1) (b). The spectrum for (9,4) is calculated along the line connecting the points $\mathbf{G}_1(9,4)$ and $\mathbf{G}_2(9,4)$. The spectrum for (2,1) is calculated in the folded (four times) reciprocal cell of the superlattice along the line connecting the points $\mathbf{G}_1(2,1)/4 \approx \mathbf{G}_1(9,4)$ and $\mathbf{G}_2(2,1)/4 \approx \mathbf{G}_2(9,4)$.

For the structure (m_r, r) and close basic structure $(m_0, 1)$ with $m_0 = [m_r/r]$, we have

$$\mathbf{G}_{1,2}(m_r, r) \approx \mathbf{G}_{1,2}(m_0, 1)/r \quad (29)$$

if $r \neq 3n$, or

$$\begin{aligned} \mathbf{G}_1(m_r, r) &\approx [\mathbf{G}_1(m_0, 1) - \mathbf{G}_2(m_0, 1)]/r, \\ \mathbf{G}_2(m_r, r) &\approx [\mathbf{G}_1(m_0, 1) + 2\mathbf{G}_2(m_0, 1)]/r \end{aligned} \quad (30)$$

otherwise. For $r \neq 3n$ we can compare the low-energy spectra of the (m_r, r) and $(m_0, 1)$ structures directly by folding the Brillouin zone of the $(m_0, 1)$ superstructure. Figure 4 shows the low-energy spectra of the structure (9,4) with $\theta = 11.985^\circ$ and the structure (2,1) having a similar twist angle $\theta = 13.174^\circ$. The spectrum for (9,4) is calculated along the line connecting the reciprocal supercell vectors of this structure: $\mathbf{G}_1(9,4)$ and $\mathbf{G}_2(9,4)$. The spectrum for (2,1) is calculated along the line connecting the points $\mathbf{G}_1(2,1)/4$ and $\mathbf{G}_2(2,1)/4$ in the reciprocal cell of the superlattice, which has been folded four times. After folding, the momenta $\mathbf{k} + i\mathbf{G}_1/4 + j\mathbf{G}_2/4$ (with

$i, j = 0, 1, 2, 3$) become equal to each other, and the number of bands increases 16 times. We see that these spectra are very similar to each other, with the single exception that the splitting of the low-energy bands for the (9,4) structure is much smaller than that for the (2,1) structure.

The direct comparison of the spectra for (m_r, r) and $(m_0, 1)$ structures with $r = 3n$ in the way described above is not possible. This is because for $r = 3n$, the folding procedure brings the Dirac points of the $(m_0, 1)$ superlattice, $\mathbf{K}_{1,2}$, to the single $\Gamma(0,0)$ point. For (m_r, r) structures, however, the Dirac points $\mathbf{K}_{1,2}$ are not equivalent to each other; their locations are given by Eq. (17). In principle, one can fold both structures in such a manner that the corresponding folded Brillouin zones coincide. However, this increases drastically the number of low-energy bands to compare. Instead, we compare the density of states (DOS) for different superstructures with close twist angles. More precisely, using numerical integration over momentum space, we calculate the density of states at finite temperature T :

$$\rho_T(E) = \frac{1}{N} \sum_i \int \frac{d^2\mathbf{k}}{v_{\text{BZ}}} \frac{1}{4T \cosh^2\left(\frac{E-E_{\mathbf{k}}^{(i)}}{2T}\right)}. \quad (31)$$

The density of states is normalized such that $\int_{-\infty}^{+\infty} dE \rho_T(E) = 1$. Typical curves (for $\theta > \theta_c$) are presented in Fig. 5 (we choose $T = 0.01t$). The DOS behaves almost linearly at small energies and has several Van Hove peaks at larger energies. The two Van Hove peaks closest to zero energy are due to the overlapping of two tBLG Dirac cones, which leads to the appearance of saddle points in the spectrum. Such a behavior of the DOS is in agreement both with theoretical studies [21,22] and STM measurements [3,4]. Comparing the curves $\rho_T(E)$ for structures with close twist angles (see Fig. 5), we find that the density of states continuously depends on θ when $T > \Delta_s$. This is not so, however, at smaller temperatures and energies very close to the chemical potential μ at zero doping. To determine the density of states in this case we have to calculate the spectrum near the Dirac points. For $r \neq 3n$ structures, the low-energy bands are described with very good accuracy by Eq. (27), while for $r = 3n$ the momentum dependence of the low-energy bands is [see Figs. 5(b) and 5(c)]

$$\begin{aligned} \bar{E}_{\mathbf{K}+\delta\mathbf{k}}^{(1,4)} &= \mu \mp \sqrt{\Delta_s^2 + v_F^2 \delta\mathbf{k}^2}, \\ \bar{E}_{\mathbf{K}+\delta\mathbf{k}}^{(2,3)} &= \mu \mp \left(\sqrt{\Delta_s^2 + v_F^2 \delta\mathbf{k}^2} - \Delta_s \right). \end{aligned} \quad (32)$$

Thus, for $r \neq 3n$ structures, the spectrum has a gap Δ , while for $r = 3n$ the spectrum is gapless, and the bands $\bar{E}_{\mathbf{K}+\delta\mathbf{k}}^{(2,3)}$ touch each other at the Dirac points. For these structures, the density of states is nonzero at the Fermi level and is proportional to the band splitting Δ_s . For energies close to the Fermi level, the density of states (at $T = 0$) for these two types of structures can be written as

$$\begin{aligned} \rho_0(E + \mu) &= \frac{a^2 \sqrt{3} |E|}{8\pi v_F^2} \left[\Theta(|E| - \Delta_s) \right. \\ &\quad \left. + \frac{v_F k_0}{\sqrt{E^2 - \Delta^2}} \Theta(|E| - \Delta) \Theta(\Delta_s - |E|) \right], \end{aligned} \quad (33)$$

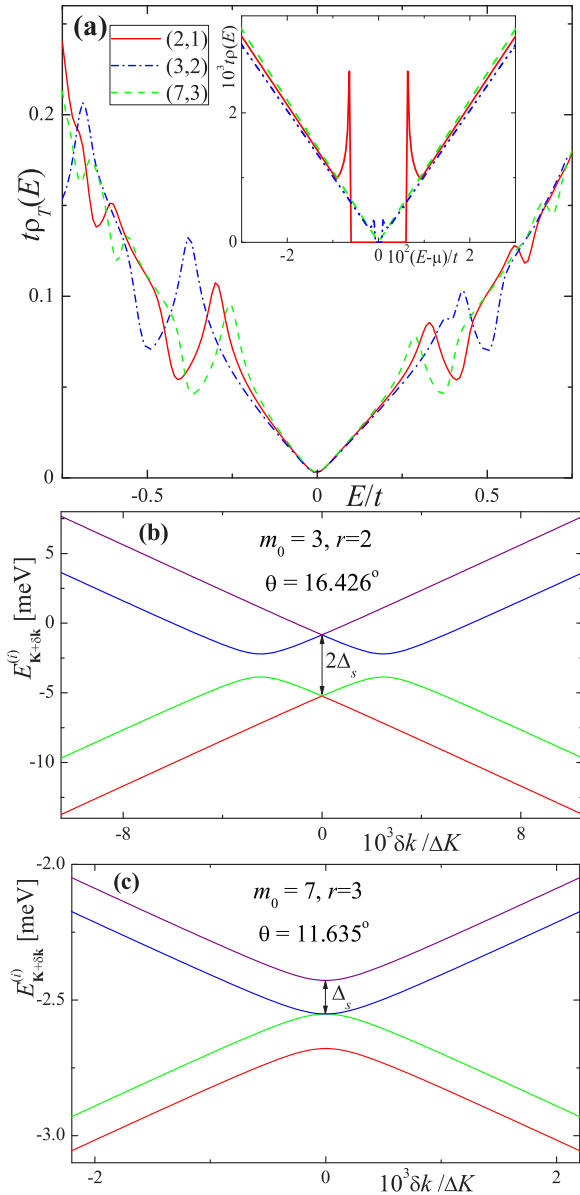


FIG. 5. (Color online) (a) Finite temperature ($T = 0.01t$) density of states $\rho_T(E)$ calculated for the superstructure (2,1) ($\theta \approx 13.174^\circ$), the superstructure (3,2) ($\theta \approx 16.426^\circ$), and the superstructure (7,3) ($\theta \approx 11.635^\circ$). The peaks in the range $0.25 < |E/t| < 0.5$ are Van Hove singularities due to the overlapping of two tBLG Dirac cones. The inset shows the zero-temperature density of states ρ calculated for energies close to the Fermi level. The structures (2,1) and (3,2) are gapped; the gap for the structure (3,2) is much lower than that for the (2,1). The structure (7,3) is gapless and has a finite density of states at the Fermi level. (b)–(c) Typical tBLG spectra close to the Dirac point for $r \neq 3n$ (b) and $r = 3n$ (c) structures. The value of the band splitting parameter Δ_s is shown by double arrows.

if $r \neq 3n$, or

$$\rho_0(E + \mu) = \frac{a^2 \sqrt{3}}{16\pi v_F^2} [|E| + \Delta_s + |E| \Theta(|E| - \Delta_s)], \quad (34)$$

if $r = 3n$.

Such a behavior of the low-energy bands for $r \neq 3n$ and $r = 3n$ structures coincides with tight-binding calculations

done in Ref. [16]. However, the low-energy approach proposed in Ref. [24] gives the opposite results: the spectrum of the $r = 3n$ system is described by Eq. (27), while for $r \neq 3n$ the band structure corresponds to Eq. (32).

The DOS at zero temperature near the Fermi level for several superstructures with nearby twist angles is shown in the inset in Fig. 5(a). At small energies, the density of states exhibits strong sensitivity to the type of structure, while for $|E - \mu| > \max(\Delta_s)$, the DOS for similar twist angles almost coincide with each other.

In the energy region, where the DOS curves coalesce, the density of states depends linearly on the energy. The proportionality coefficient is set by the Fermi velocity, which is determined by fitting the numerically calculated spectrum with either Eqs. (27) or (32) (the choice between these two equations is based on the structure type). For several $r \neq 1$ structures, whose twist angles are close to the twist angle θ of the (2,1) structure, the Fermi velocity is shown as circles in Fig. 3. We see that the Fermi velocities of the $r = 1$ and $r \neq 1$ structures are well described by a single smooth curve monotonously decreasing with decreasing twist angle.

Thus, our analysis indicates that the density of states at finite temperatures (for $T > \Delta_s$) and the Fermi velocity can be considered as continuous functions of the twist angle. The band splitting, and even the type of $T = 0$ low-energy spectrum, however, are very sensitive to the type of superstructure, and can vary significantly for structures with arbitrary close twist angles. Let us discuss this issue in more details. In Fig. 6 we plot the band splitting Δ_s as a function of the twist angle θ for all superstructures, whose supercell contains $N < 2000$ atoms. It is seen from this figure that Δ_s is not a monotonous function

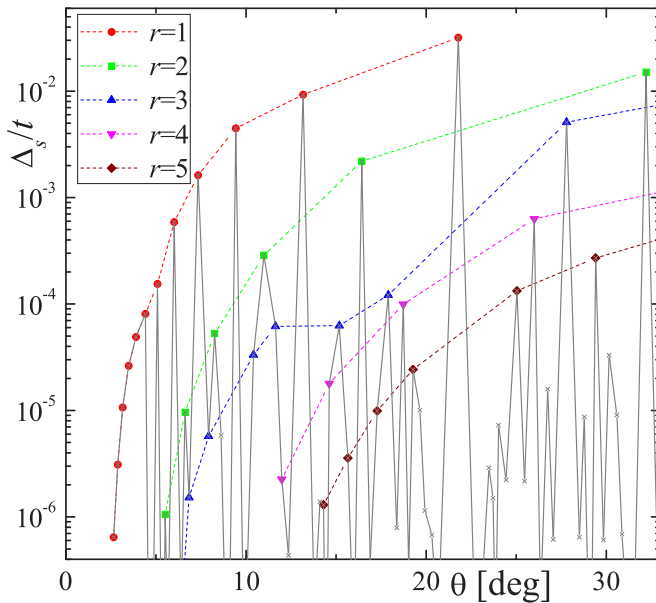


FIG. 6. (Color online) The band splitting Δ_s as a function of the twist angle θ calculated for all superstructures with $N < 2000$ (gray solid line). Different dashed curves connect the points corresponding to superstructures with the same value of r . We can see that, if r is fixed, the band splitting decreases monotonously as m_0 grows (when m_0 grows, the angle θ decreases). However, when r is not restricted, the splitting Δ_s can change exponentially for weak variations of θ .

of θ : any small deviation of the twist angle from a given value changes drastically the band splitting. However, there is some order in this chaos: the band splitting Δ_s for superstructures with fixed r monotonously decreases when the twist angle decreases. All curves Δ_s versus θ at fixed r are qualitatively similar to each other, and the curve for $r = 1$ superstructures lies above all other curves.

Thus, among all possible superstructures in some range of twist angles, the maximum band splitting corresponds to the $r = 1$ superstructure. According to our calculations, for $m_0 < 7$ the band splitting exceeds 1 K, which is experimentally observable.

However, the discontinuous behavior of Δ_s versus θ makes the direct interpretation of the graph in Fig. 6 problematic. After all, in any realistic situation the twist angle is known with finite error. Examining Fig. 6 we discover that within a given small interval of θ one can find an exponentially wide range of band splittings.

To resolve this paradox one must remember that the data in Fig. 6 are valid only for infinite and ideally clean samples with infinite mean-free path. In an experimental situation these assumptions are not valid. Let us denote a length scale \tilde{L} characterizing the coherent motion of electrons in the tBLG. This scale can be limited by the sample size for mesoscopic samples, or the mean-free path of electrons scattered by impurities, “topological defects” (e.g., “the wrinkles” due to spacial variation of the twist angle), phonons, etc.

Imagine now that the twist angle deviates from the value θ_0 corresponding to the $(m_0, 1)$ superstructure by some small quantity $\delta\theta$. Using Eqs. (5)–(8), one can show that the minimal supercell size L_{sc} among all $r \neq 1$ superstructures inside this angular interval can be estimated as

$$\frac{L_{sc}}{a} \sim \frac{\theta_0}{|\delta\theta|}. \quad (35)$$

Our calculations of the spectrum and the band splitting are relevant only when $\tilde{L} \gg L_{sc}$. Thus, the results for Δ_s presented here are not applicable for

$$|\delta\theta| \lesssim \theta_0 \frac{a}{\tilde{L}}. \quad (36)$$

Inside this region of twist angles we should take into account the influence of the electron scattering or the sample’s size on the band gap and band splitting. We expect that this will lead to a continuous dependence of Δ on θ .

To verify this we diagonalized the Hamiltonian (18) for finite-size samples. The sample has the shape of a rhombus with sides \tilde{L} and an acute angle between sides equal to 60° . The rotation of the layer 2 is performed around the central point of the sample, where the A1 and B2 carbon atoms are located. We now choose $(m_0, r) = (1, 1)$, which corresponds to $\theta_0 \cong 21.787^\circ$, as a reference structure. The sample size should be large enough in order to suppress the size-quantization effect. At small energies, the energy difference between neighboring electron states is about v_F/\tilde{L} . Thus, the parameter \tilde{L} must satisfy the inequality

$$\tilde{L}/a \gg v_F/(a\Delta) \sim t/\Delta \approx 30$$

for $t = 2.57$ eV, and the gap $\Delta \cong 0.08$ eV corresponding to the (1, 1) structure.

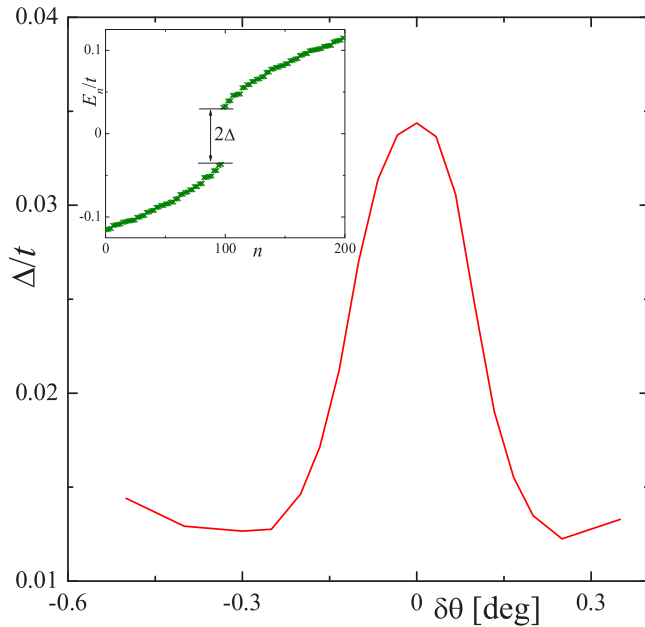


FIG. 7. (Color online) Dependence of the band gap Δ on the deviation $\delta\theta$ of the twist angle from the value $\theta(1,1) \cong 21.787^\circ$, calculated for finite sample of rhombic shape containing 151×151 unit cells in each graphene layer. The total number of atoms in the sample $N_{\text{atoms}} = 91\,204$. The inset shows the energy distribution of the first 200 electron levels close to the zero energy, calculated for $\delta\theta = 0$.

In addition to the size-quantization effect, we must deal with another complication: the emergence of low-energy states localized at the sample edges. To eliminate them an extra term is added to the Hamiltonian: we introduce the potential-energy difference between A and B atoms which decays exponentially fast away from the edge. This “boundary condition” pushes the edge states eigenenergies out of the low-energy range.

The band gap of the finite-size sample as a function of the deviation $\delta\theta$ from the twist angle θ_0 is shown in Fig. 7. We see that Δ decreases continuously from its maximum at $\delta\theta = 0$ down to the background nonzero value set by the size quantization.

The calculations for samples of different sizes ($\tilde{L}/a = 61, 75, 151$) show that the characteristic width of the peak, $\overline{\Delta\theta}$, satisfies the relationship

$$\overline{\Delta\theta}\tilde{L}/a \sim 1.$$

In other words, the gap disappears when the maximum deviations in the positions of the atoms in the sample $\tilde{L}\delta\theta$ is about a lattice constant. The larger the value of \tilde{L} , the smaller fluctuations in the twist angle destroy the band gap.

We expect that similar results are also valid for an infinite, but nonideal sample with a finite mean-free path of electrons. If this so, we would have a paradoxical situation: the fewer defects the sample has, the more difficult it would be to experimentally observe the gap in the spectrum due to the fluctuations of the twist angle. This issue, as well as the study of the effects of other possible fluctuations in the tBLG crystal lattice, are beyond the scope of this work.

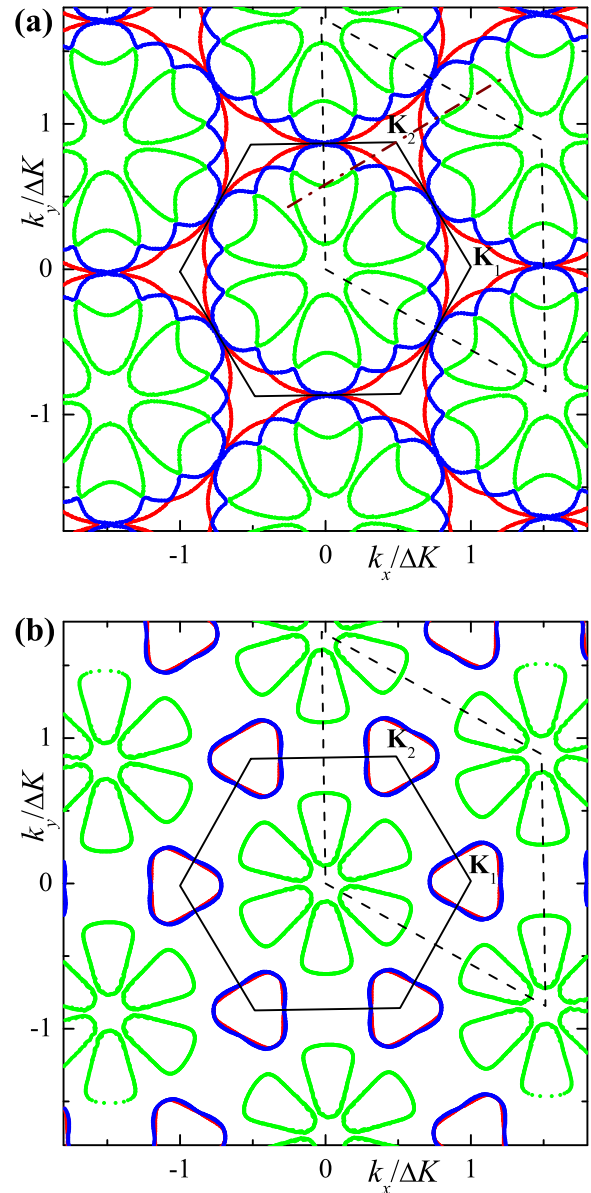


FIG. 8. (Color online) Fermi surfaces of the superstructures $(17,1)$ [$\theta \cong 1.89^\circ$, (a)] and $(18,1)$ [$\theta \cong 1.79^\circ$, (b)] calculated at half filling. Different colors correspond to different bands intersecting the Fermi level μ at half filling. The first Brillouin zone (hexagon) and the reciprocal supercell (rhombus) are also shown. The dot-dashed line in (a) shows the way along which the spectrum presented in Fig. 2(f) is calculated.

V. SMALL TWIST ANGLE $\theta < \theta_c$

The Fermi velocity v_F calculated according to Eq. (27) decreases when θ decreases (see Fig. 3), in good agreement with previous theoretical [13–15,17,19,21–23], and experimental [1,5] studies. For angles close to $\theta_c = 1.89^\circ$, four low-energy bands become almost flat in the whole Brillouin zone, with the exception of the small region near the point Γ [see Figs. 2(a)–2(c)]. In the region of twist angles $\theta_c \cong 1.89^\circ < \theta \lesssim 4.4^\circ$, the band splitting is too small to be experimentally observable even for $r = 1$ superstructures. Since the band

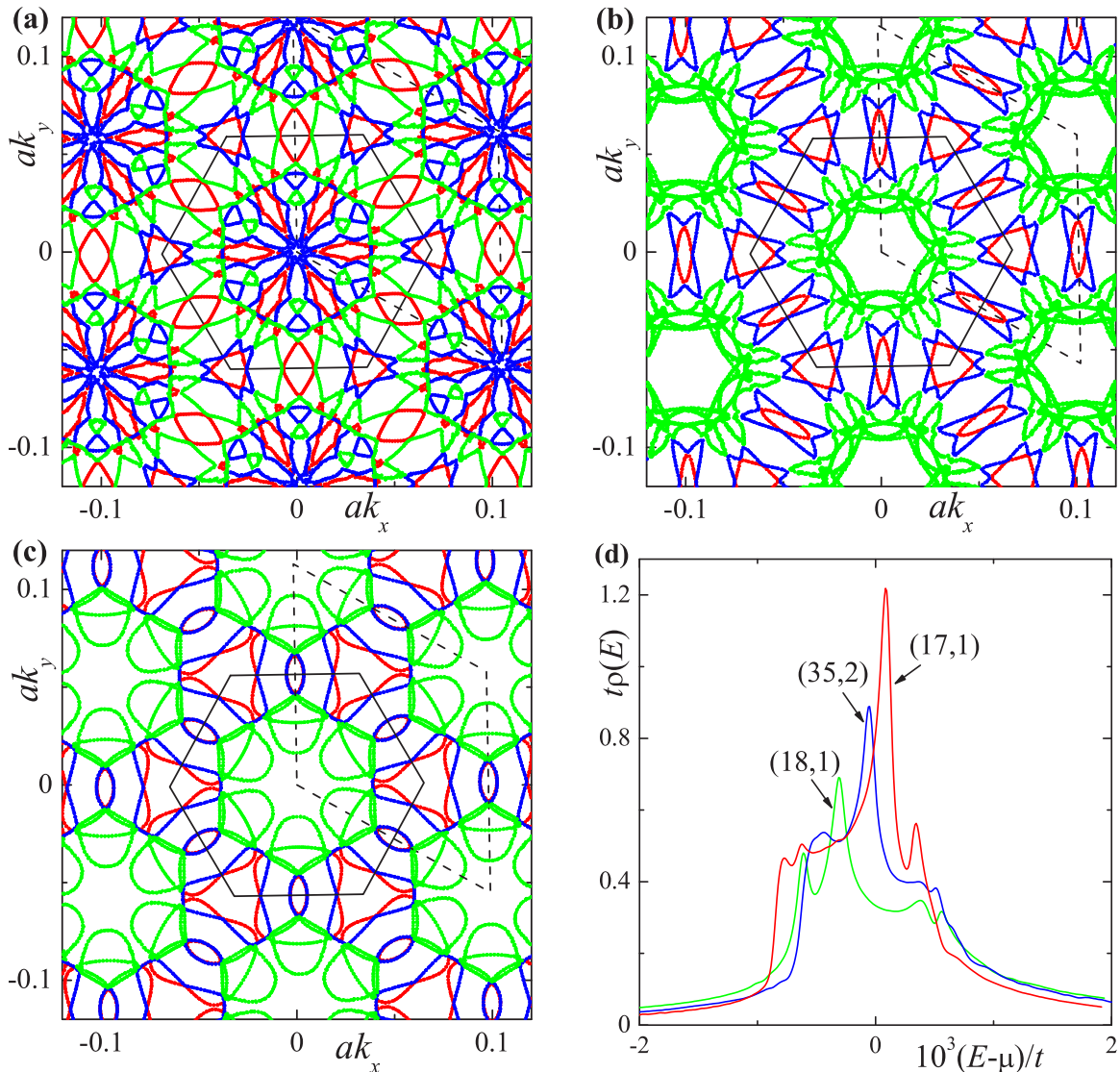


FIG. 9. (Color online) Fermi surfaces of the superstructures (17,1) [$\theta \cong 1.89^\circ$, (a)], (35,2) [$\theta \cong 1.84^\circ$, (b)], and (18,1) [$\theta \cong 1.79^\circ$, (c)] calculated at half filling. The Fermi surfaces for the structures (17,1) and (18,1) are calculated by band folding of the original Fermi surfaces. Different colors correspond to different bands intersecting the Fermi level μ at half filling. Panels (a) and (c) show the same Fermi surfaces as Figs. 8(a) and 8(b), but in the folded Brillouin zone. (d) The low-energy density of states calculated for three superstructures with similar twist angles $\theta < \theta_c$. The density of states is calculated at finite temperature $T/t = 10^{-5}$ by numerical integration over the momentum; see Eq. (31). Note that in units of t the energy window where the weight is enhanced is very narrow.

splitting is negligible, the density of states changes continuously with the twist angle.

For smaller angles, $\theta < \theta_c$ ($m_0 \geq 17$), the conelike shape of the low-energy bands completely disappears even near the Dirac points [see Fig. 2(f)], the gap becomes zero, and the system acquires a Fermi surface and nonzero density of states at the Fermi level. As θ decreases further, the Fermi surface changes, and for some values of θ reduces to several Fermi points. The density of states at the Fermi level oscillates with θ .

Figure 8 shows the Fermi surfaces calculated at half filling for the superstructures (17,1) corresponding to $\theta_c \cong 1.89^\circ$ and similar to the structure (18,1) ($\theta \cong 1.79^\circ$). It is clearly seen from these figures that the Fermi surfaces are similar to each other, and the total size (length) of the Fermi surface sheets for the structure (18,1) is smaller than that for the (17,1). The band

flatness, the nonzero density of states for small θ , as well as the existence of the “magic” angles where the density of states vanishes is consistent with many previous studies using both low-energy [22,23,26] and tight-binding calculations [13,17–19].

Our calculations show that no gap exists between the low-energy bands and the lower or upper bands. Thus, the system remains metallic under doping when the chemical potential shifts from its values at half filling. On the other hand, the bands $\bar{E}_{\mathbf{k}}^{(v)}$ are quite flat if $\theta < \theta_c$; the Fermi velocities are about 10^{-3} times smaller than those for a single graphene layer. Consequently, the disorder or the electron-electron interaction may qualitatively change the metallic band structure giving rise to localization or opening of a gap due to ordering.

The superstructures with $r \neq 1$ are also metallic if θ is smaller than θ_c . To compare the Fermi surfaces, we perform

band folding for $r = 1$ superstructures as described in Sec. IV B. Figure 9 shows the Fermi surfaces for the superstructures (17,1) [$\theta \cong 1.89^\circ$, panel (a)] and (18,1) [$\theta \cong 1.79^\circ$, panel (c)] calculated in the folded (reduced two times in size) Brillouin zones, as well as the Fermi surface for the intermediate (35,2) [$\theta \cong 1.84^\circ$, panel (b)] superstructure. Since the twist angles are quite small, the Brillouin zones considered almost coincide with each other. All Fermi surfaces are calculated at half filling, and the position of the chemical potential μ in each case is found in the way described in Sec. III. We see that the Fermi surface of the intermediate $r = 2$ superstructure, being different in some details, contains, however, all basic elements presented in the Fermi surface (in folded Brillouin zones) of both proximate $r = 1$ superstructures.

For a more quantitative analysis, we calculate the low-energy density of states of $r = 1$ and $r \neq 1$ superstructures with similar twist angles. The densities of states near the Fermi level for the (17,1), (35,2), and (18,1) superstructures are shown in Fig. 9(d). Each density of states has a sharp peak and a shoulder, which has additional smaller peaks. The height and the position of the central peak with respect to the Fermi level, as well as the height and the position of the shoulder, correlate with the change of the twist angle. For the superstructure (m_r, r) with $\theta < \theta_c$, the number of low-energy bands which contribute to the peaks and shoulder in the density of states at low energies is equal to $n_0 = 4r^2/g$, where $g = 1$ if $r \neq 3n$ or $g = 3$ otherwise. With the normalization of the DOS used in Eq. (31), the integral of $\rho_T(E)$ over low energies [the area under the curves shown in Fig. 9(d)] with a high accuracy is equal to $S = 4r^2/[gN(m_r, r)]$. Using Eqs. (5) and (8), one can easily show that this integral depends only on the twist angle and is equal to

$$S = \sin^2 \frac{\theta}{2}. \quad (37)$$

The spectral weight shifts toward higher energies as the twist angle decreases.

Thus, our analysis of the DOS and the Fermi surface indicates that neglecting some delicate details, the electronic properties of the tBLG change continuously with the twist angle when $\theta < \theta_c$. However, further analysis is required to address the issues of the evolution of the Fermi surface at very small angles (e.g., the existence of the magic angles where the Fermi surface vanishes, etc.).

VI. CONCLUSIONS

To conclude, we have studied a tight-binding model for twisted bilayer graphene in a wide range of twist angles. In the model Hamiltonian we take into account the effect of the environment-dependent hopping, which correctly reproduces the Slonczewski-Weiss-McClure scheme for interlayer hopping amplitudes in bilayer graphene. We demonstrate that at twist angles $\theta > \theta_c \cong 1.89^\circ$ the tBLG can have a band gap, which can be as large as 80 meV. The gap is maximum for twist angles corresponding to superstructures with the superlattice period coinciding with their Moiré period. This gap, however, is very sensitive to small deviations of the twist angle from these original values. This sensitivity of the gap disappears for finite-size samples. If θ is below a critical angle θ_c , tBLG has a Fermi surface, and the DOS has a peak at the Fermi level. Moreover, the DOS changes continuously with the twist angle.

ACKNOWLEDGMENTS

The authors are grateful to A. N. Sergeev-Cherenkov for computing assistance. This work was supported in part by the RFBR (Grants No. 14-02-00276, No. 14-02-00058, No. 12-02-00339), the Russian Science Support Foundation, the RIKEN iTHES Project, MURI Center for Dynamic Magneto-Optics, and a Grant-in-Aid for Scientific Research (S).

-
- [1] A. Luican, G. Li, A. Reina, J. Kong, R. R. Nair, K. S. Novoselov, A. K. Geim, and E. Y. Andrei, *Phys. Rev. Lett.* **106**, 126802 (2011).
 - [2] L. Brown, R. Hovden, P. Huang, M. Wojcik, D. A. Muller, and J. Park, *Nano Lett.* **12**, 1609 (2012).
 - [3] I. Brihuega, P. Mallet, H. González-Herrero, G. Trambly de Laissardière, M. M. Ugeda, L. Magaud, J. M. Gómez-Rodríguez, F. Yndurán, and J.-Y. Veuillen, *Phys. Rev. Lett.* **109**, 196802 (2012).
 - [4] W. Yan, M. Liu, R.-F. Dou, L. Meng, L. Feng, Z.-D. Chu, Y. Zhang, Z. Liu, J.-C. Nie, and L. He, *Phys. Rev. Lett.* **109**, 126801 (2012).
 - [5] Z. Ni, Y. Wang, T. Yu, Y. You, and Z. Shen, *Phys. Rev. B* **77**, 235403 (2008).
 - [6] R. W. Havener, H. Zhuang, L. Brown, R. G. Hennig, and J. Park, *Nano Lett.* **12**, 3162 (2012).
 - [7] T. Ohta, J. T. Robinson, P. J. Feibelman, A. Bostwick, E. Rotenberg, and T. E. Beechem, *Phys. Rev. Lett.* **109**, 186807 (2012).
 - [8] K. S. Kim, A. L. Walter, L. Moreschini, T. Seyller, K. Horn, E. Rotenberg, and A. Bostwick, *Nat. Mater.* **12**, 887 (2013).
 - [9] D. S. Lee, C. Riedl, T. Beringer, A. H. Castro Neto, K. von Klitzing, U. Starke, and J. H. Smet, *Phys. Rev. Lett.* **107**, 216602 (2011).
 - [10] J. D. Sanchez-Yamagishi, T. Taychatanapat, K. Watanabe, T. Taniguchi, A. Yacoby, and P. Jarillo-Herrero, *Phys. Rev. Lett.* **108**, 076601 (2012).
 - [11] A. N. Kolmogorov and V. H. Crespi, *Phys. Rev. B* **71**, 235415 (2005).
 - [12] S. Latil, V. Meunier, and L. Henrard, *Phys. Rev. B* **76**, 201402(R) (2007).
 - [13] S. Shallcross, S. Sharma, and O. Pankratov, *Phys. Rev. B* **87**, 245403 (2013).
 - [14] S. Shallcross, S. Sharma, E. Kandelaki, and O. A. Pankratov, *Phys. Rev. B* **81**, 165105 (2010).
 - [15] W. Landgraf, S. Shallcross, K. Türschmann, D. Weckbecker, and O. Pankratov, *Phys. Rev. B* **87**, 075433 (2013).
 - [16] S. Shallcross, S. Sharma, and O. A. Pankratov, *Phys. Rev. Lett.* **101**, 056803 (2008).
 - [17] G. Trambly de Laissardière, D. Mayou, and L. Magaud, *Nano Lett.* **10**, 804 (2010).

- [18] G. Trambly de Laissardière, D. Mayou, and L. Magaud, *Phys. Rev. B* **86**, 125413 (2012).
- [19] E. Suárez Morell, J. D. Correa, P. Vargas, M. Pacheco, and Z. Barticevic, *Phys. Rev. B* **82**, 121407(R) (2010).
- [20] E. J. Mele, *J. Phys. D* **45**, 154004 (2012).
- [21] J. M. B. Lopes dos Santos, N. M. R. Peres, and A. H. Castro Neto, *Phys. Rev. Lett.* **99**, 256802 (2007).
- [22] J. M. B. Lopes dos Santos, N. M. R. Peres, and A. H. Castro Neto, *Phys. Rev. B* **86**, 155449 (2012).
- [23] R. Bistritzer and A. H. MacDonald, *Proc. Natl. Acad. Sci. USA* **108**, 12233 (2011).
- [24] E. J. Mele, *Phys. Rev. B* **81**, 161405(R) (2010).
- [25] E. J. Mele, *Phys. Rev. B* **84**, 235439 (2011).
- [26] P. San-Jose, J. González, and F. Guinea, *Phys. Rev. Lett.* **108**, 216802 (2012).
- [27] M. S. Tang, C. Z. Wang, C. T. Chan, and K. M. Ho, *Phys. Rev. B* **53**, 979 (1996).
- [28] J. W. McClure, *Phys. Rev.* **108**, 612 (1957); J. C. Slonczewski and P. R. Weiss, *ibid.* **109**, 272 (1958).
- [29] E. Mendez, A. Misu, and M. S. Dresselhaus, *Phys. Rev. B* **21**, 827 (1980).
- [30] M. Mucha-Kruczynski, O. Tsypliyatyev, A. Grishin, E. McCann, V. I. Fal'ko, A. Bostwick, and E. Rotenberg, *Phys. Rev. B* **77**, 195403 (2008).
- [31] M. S. Dresselhaus and G. Dresselhaus, *Adv. Phys.* **51**, 1 (2002).
- [32] We take $R_{ij} = r_{ij}$ in Eq. (2) of Ref. [27] since, with a high accuracy, the effective coordination numbers g_i in Eq. (4) of Ref. [27] turn out to be the same for all sites. As a result, we obtain $R_{ij} = Cr_{ij}$, and the constant C is absorbed in the coefficients α_1 and α_4 .
- [33] We use the ARPACK package, which can be downloaded from <http://www.caam.rice.edu/software/ARPACK/>. Additional instructions for Windows users can be found, e.g., in <http://www.cs.cmu.edu/~barbic/arpac.html>.